

Axisymmetric Schwarzschild models of an isothermal axisymmetric mock dwarf spheroidal galaxy.

Jorrit H.J. Hagen, Amina Helmi, and Maarten A. Breddels

Kapteyn Astronomical Institute, University of Groningen, P.O. Box 800, 9700 AV Groningen, The Netherlands
e-mail: hagen@astro.rug.nl

Received 27 Jun 2019 / Accepted DD Mon YYYY

ABSTRACT

Aims. The goal of this work is to test the ability of Schwarzschild’s orbit superposition method in measuring the mass content, scale radius and shape of a flattened dwarf spheroidal galaxy. Until now, most dynamical model efforts have assumed that dwarf spheroidal galaxies and their host halos are spherical.

Methods. We use an Evans model (1993) to construct an isothermal mock galaxy whose properties somewhat resemble those of the Sculptor dwarf spheroidal galaxy. This mock galaxy contains flattened luminous and dark matter components, resulting in a logarithmic profile for the global potential. We have tested how well our Schwarzschild method could constrain the characteristic parameters of the system for different sample sizes, and also if the functional form of the potential was unknown.

Results. When assuming the true functional form of the potential, the Schwarzschild modelling technique is able to provide an accurate and precise measurement of the characteristic mass parameter of the system and reproduces well the light distribution and the stellar kinematics of our mock galaxy. When assuming a different functional form for the potential, such as a flattened NFW profile, we also constrain the mass and scale radius to their expected values. However in both cases, we find that the flattening parameter remains largely unconstrained. This is likely because the information content of the velocity dispersion on the geometric shape of the potential is too small, since σ is constant across our mock dSph.

Conclusions. Our results using Schwarzschild’s method indicate that the mass enclosed can be derived reliably, even if the flattening parameter is unknown, and already for samples containing 2000 line-of-sight radial velocities, such as those currently available. Further applications of the method to more general distribution functions of flattened systems are needed to establish how well the flattening of dSph dark halos can be determined.

Key words. dark matter – Galaxies: dwarf – Galaxies: kinematics and dynamics

1. Introduction

In the current cosmological Λ CDM model most of the mass is believed to be in the form of (cold) dark matter. While successful on large scales, on the scales of dwarf galaxies, the model suffers a number of challenges, including the missing satellites problem (Klypin et al. 1999; Moore et al. 1999), the cusp-core conundrum (Hui 2001), and the too big to fail problem (Boylan-Kolchin et al. 2011), although all may be solved one way or another by considering the effects of baryonic physics (e.g. Zolotov et al. 2012; Brooks et al. 2013; Wetzel et al. 2016; Kim et al. 2018). The dwarf spheroidal satellite galaxies (dSph’s or dSph galaxies) of our Milky Way can provide particularly strong constraints on the nature of dark matter, since their high mass-to-light ratios suggest that they are fully dark matter dominated (Strigari et al. 2008; Walker et al. 2007; Wolf et al. 2010).

Various methods have been used to develop dynamical models of dSph galaxies using line-of-sight velocity measurements for large samples of individual stars in these systems (e.g. Battaglia et al. 2006, 2008a,b, 2011; Walker et al. 2009a, 2015). Modelling via the Jeans Equations, distribution functions, and orbit superposition methods like Schwarzschild modelling are amongst those most often used (Battaglia et al. 2013). All these methods have in common that they assume that the systems are in dynamical equilibrium.

The Jeans Equations are derived by taking moments of the Collisionless Boltzmann Equation, which itself describes the conservation of probability in phase-space (Binney & Tremaine 2008). Not every solution of the Jeans equations has an associated distribution function that is physical (i.e. positive) everywhere. Furthermore finding a solution requires additional assumptions, for example on the functional form of the density profile and on the velocity anisotropy (because this is generally not known, although see the work by Massari et al. 2018, who determined directly the anisotropy of a sample of stars in the Sculptor dSph using proper motions derived from *Gaia* and HST). Because Jeans modelling is very flexible and fast it has become the most widely used tool to model dSph galaxies, particularly in the spherical limit. It has, for example, allowed for a robust (independent of the velocity anisotropy) measurement of the mass enclosed within approximately the half light radii of the dSph galaxies (Walker et al. 2009b; Wolf et al. 2010), and the determination that the masses of the classical dSph’s are in the range $\sim (10^8 - 10^9)M_{\odot}$ (e.g. Walker et al. 2007). On the other hand, it has not been possible to rule out cusped or cored profiles on the basis of these types of models (e.g. Evans et al. 2009; Strigari et al. 2017).

The Schwarzschild (1979) modelling technique relies on the idea that a system can be seen as a superposition of stellar orbits. In Schwarzschild modelling one only needs to assume a specific gravitational potential form. The method does require a signifi-

cant amount of computing power and therefore a smaller set of gravitational potentials can be explored in comparison to Jeans modelling. Breddels & Helmi (2013) have applied this method to 4 dwarf spheroidal galaxies and by modelling both the second and fourth line-of-sight velocity moments and assuming spherical symmetry they find that, independently of the particular form assumed for the potential, it is possible to constrain not only the mass at around the half-light radius (more precisely at r_{-3} where the logarithmic slope of the luminous density is -3) but also the logarithmic slope of the dark matter density.

Most work thus far has assumed that dwarf spheroidal galaxies and their host halos are spherical, despite the fact that their light distribution is typically not round (Irwin & Hatzidimitriou 1995; McConnachie 2012). Furthermore, dark matter halos are predicted to be triaxial (Jing & Suto 2002) when no baryonic effects are taken into account, although subhalos in cold dark matter simulations that could host dSph's are only mildly triaxial, and almost axisymmetric (Vera-Ciro et al. 2014). This implies that it is important to establish how many and which of the previously mentioned results still stand when taking into account deviations from spherical symmetry.

Kowalczyk et al. (2017, 2018) have in fact studied the ability of recovering the mass profile and anisotropy of the remnants of the mergers of dwarf disk galaxies (one postulated channel for the formation of dSph) when using spherical Schwarzschild models. These authors have shown that for spherical remnants the method can break the mass-anisotropy degeneracy, whereas for non-spherical (prolate) remnants the anisotropy will always be underestimated, although the total mass profile will be recovered well for data along the minor axis (although not if the data are along the major axis).

On the other hand, Hayashi & Chiba (2012, 2015) used axisymmetric Jeans modelling to infer the axis ratio of the dark matter density distribution (Q) in several dSph's assuming a constant velocity anisotropy β_z . They report rather low axis ratios ($Q = [0.3 - 0.5]$) compared to the observed projected flattening in the light ($q'_* \sim 0.7$). These low values are somewhat counterintuitive, though the results may be affected by degeneracies between Q , the velocity anisotropy profile, the viewing angle of the dSph, and the inner slope of the dark matter density profile. In Hayashi et al. (2016), a very similar technique was applied to unbinned data, and for e.g. Scl dSph, the authors found that the flattening parameter is largely unconstrained.

In this work we explore the performance of the Schwarzschild modelling technique in the axisymmetric regime, to free ourselves from the assumptions inherent to Jeans models. We test the method on a mock Sculptor-like dSph and consider axisymmetric mass distributions for both the light and the dark matter component and establish how well the characteristic parameters of the potential can be recovered, for different sample sizes.

The paper is organised as follows. In Sect. 2, we set up a mock galaxy and simulate a realistic dataset. In Sect. 3 we describe the Schwarzschild method and its implementation in this work. Then, in Sect. 4.1, we apply the Schwarzschild method and show that we can recover the characteristic mass parameter of the mock galaxy potential, irrespective of the potential flattening assumed. In Sect. 4.2 we model our mock galaxy with an axisymmetric NFW potential form and show that, even in this case, the Schwarzschild method is able to constrain the mass and scale radius to the expected values for datasets containing a realistic number of stars. We present our conclusions in Sect. 5 where we also discuss our findings.

2. The mock galaxy

2.1. Potential, luminous density and characteristic parameters

We have built a mock galaxy inspired in the Sculptor dSph. We have assumed a flattened stellar density profile ($q_* = 0.8$), no net rotation and a line-of-sight velocity dispersion of ~ 10 km/s (Mateo 1998; Battaglia et al. 2008a; Walker et al. 2009b). For simplicity, we have set up the mock galaxy following Evans (1993), who uses an elementary distribution function to describe a composite axisymmetric system. This distribution function is ergodic, i.e. it leads to a velocity ellipsoid that is isotropic and has a constant amplitude and thus is not generic¹.

The gravitational potential of the composite system as a whole follows the form

$$\Phi_E(R, z) = \frac{1}{2} v_0^2 \ln \left(R_c^2 + R^2 + \frac{z^2}{q^2} \right) + \Phi_0, \quad (1)$$

where (R, ϕ, z) denote the cylindrical coordinates. Here v_0^2 relates to the mass of the system and R_c is the core radius. The parameter q is the axial ratio, and has to satisfy $1/\sqrt{2} = 0.707 \leq q \leq 1.08$ where the lower limit is set by the condition that the spatial density is positive everywhere (Binney & Tremaine 2008) and the upper limit yields a composite distribution function of the form used by Evans (1993) that is positive everywhere. The zero point of the potential is set by Φ_0 .

The density profile of the stellar component is described by

$$\rho_{\text{lum}}(R, z) = \frac{\rho_0 R_c^p}{\left(R_c^2 + R^2 + z^2/q^2 \right)^{p/2}}, \quad (2)$$

where ρ_0 is the central density, p denotes a slope parameter, and q_* is the flattening of the stellar density. The associated stellar distribution function is given by

$$f_{\text{lum}}(E) \propto \exp[-pE/v_0^2] = \exp[-p\Phi_E/v_0^2] \exp[-pv^2/2v_0^2], \quad (3)$$

where E is the sum of the gravitational potential and kinetic energies of a star.

In the Evans model $q_* = q$ and therefore the density flattening of the luminous component is the same as the potential (not the density) flattening of the composite system. The surface brightness profile of the mock galaxy can be found by integrating the luminous density along the line-of-sight.

The line-of-sight velocity profile is exactly Gaussian with a velocity dispersion that is isotropic and constant everywhere:

$$\sigma_E = \frac{v_0}{\sqrt{p}}, \quad (4)$$

and independent of the inclination, scale radius and flattening.

We choose here $v_0 = 20$ km/s, $R_c = 1$ kpc, $q = 0.8$, and $p = 3.5$ for our mock galaxy. These values result in a velocity dispersion of roughly 10.7 km/s. For these values of p and q , the central total density should be at least 1.13 times the central stellar density to yield positive phase-space densities for both the stellar and dark components everywhere.

In Fig. 1 we show the 2D surface brightness profile of the mock galaxy for an edge-on view. Since the galaxy is axisymmetric, we only show the positive quadrant. Contours of constant

¹ nor is this distribution function ideal as we shall see later in the paper, because it provides very little information on the symmetries of the system.

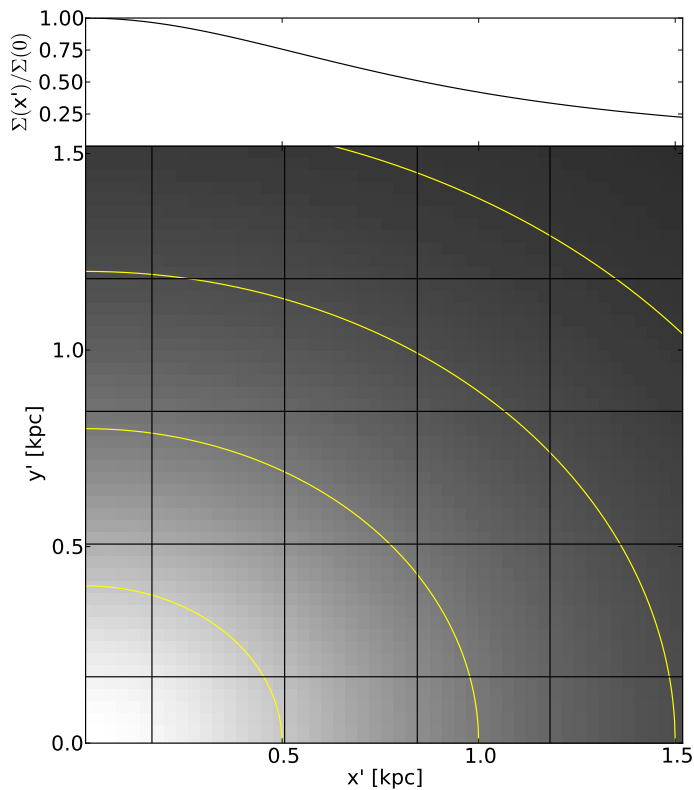


Fig. 1. The surface brightness profile of our mock galaxy in an edge-on view. The black horizontal and vertical lines show the boundaries of the kinematic-bins. We only show the positive quadrant of our FOV ($x' > 0$ kpc, $y' > 0$ kpc). The yellow contours correspond to the isophotes of the system ($q_* = q = 0.8$). In the top panel we have plotted the surface brightness normalised to its central value as function of x' , i.e. along the (projected) major axis of the galaxy.

surface brightness follow ellipses with axial ratios q'_* , which because of the edge-on view are identical to the intrinsic density flattening (i.e. $q'_* = q_* = 0.8$). The 1D surface brightness profile along the major axis is plotted in the top panel of this figure. The surface brightness decreases a factor two with respect to its central value at a projected ellipsoidal radius of 0.86 kpc, however, the projected half light radius is much larger (3.87 kpc).

2.2. Observing the mock galaxy

We generate the mock galaxy by drawing positions following the luminous density distribution (see Eq. 2) and velocities from the Gaussian distribution function (see Eq. 3). We thus assume that the dataset of the stars with line-of-sight velocities follows the same distribution as the light. We place the mock galaxy at a distance of 80 kpc, and “observe” it with a square field of view (FOV), centred on the mock galaxy, with a size of $7832'' \times 7832''$ (which then corresponds to roughly 3×3 kpc). Throughout this work we assume an edge-on view.

The typical line-of-sight velocity measurements of individual stars have errors of order $dv = 2$ km/s (Battaglia et al. 2008b; Walker et al. 2009a). Therefore, to simulate a realistic dataset we convolve the line-of-sight velocities with a Gaussian distribution having a standard deviation of 2 km/s. We compute velocity moments by combining the velocities of all available stars in a certain spatial bin on the sky (in what follows a *kinematic-bin*) in our FOV. The velocity moments are estimated by correcting for the measurement errors (see Appendix A), similarly to Breddels

et al. (2013). We assume that the surface brightness profile can be measured without error in much smaller spatial bins on the sky (which we refer to as *light-bins*). To produce a reasonable galaxy, we also assume that the three-dimensional light distribution is known to much larger radii, but for many fewer bins (more details can be found in Sect. 3.1).

3. The Schwarzschild orbit superposition method

In Schwarzschild modelling, orbits are used as building blocks of a dynamical system. Given a potential Φ , a complete set of orbits are integrated numerically and for each orbit the predicted observables are stored in a so-called orbit library. Varying the parameters of the potential (or varying the potential form as a whole), will result in different libraries. The library which provides a combination of weighted orbits that matches the observations (light profile + kinematics) best, will be said to yield the best-fit parameters of the potential. The orbital weights themselves provide the corresponding distribution function. Since the orbital weights are positive by construction, the distribution function will be non-negative everywhere.

3.1. Generating orbit libraries

In this paper we use a slightly modified version of the Schwarzschild code from van den Bosch et al. (2008), who modelled the elliptical galaxy NGC4365. In what follows, we shortly describe how we generated the orbit libraries, how the orbital integration has been done and how the libraries are stored. For more information we refer the reader to van den Bosch et al. (2008)².

Given an energy E_i , initial positions x_0 and z_0 are sampled on a open polar grid, which is defined by N_{I_2} polar angles and N_{I_3} radii in between a thin orbit and the equipotential. The polar angles are sampled linearly, but to obtain a better sampling of orbits near the major axis of the system, 50% of the polar angles are sampled from the z -axis towards 10° above the midplane, and the remaining 50% from 10° down to the $z = 0$ plane. The initial y -coordinates and initial velocities in the x - and z -directions are set to zero. The initial velocities in the y -direction, $v_{y,0}$, are determined by $E_i - \Phi(x_0, 0, z_0) = 0.5v_{y,0}^2$. This is done for all N_{ener} energies, which are defined by $E_i = \Phi(x = x_i, y = 0, z = 0)$. The locations x_i that fix the energy grid are logarithmically sampled between 25 pc and 50 kpc from the centre. This ‘orbit library’ thus consists of $N_{\text{orb}} = N_{\text{ener}} \times N_{I_2} \times N_{I_3}$ orbits (z -tubes in our axisymmetric potential).

To account for slowly precessing orbits in the library we also compute 17 copies of each orbit, where each copied orbit is subsequently rotated by 10° in the xy -plane. These 18 copies are summed into a single orbit and replace the non-rotated orbit, such that each orbit now follows the axisymmetric requirements. Besides ensuring axisymmetric behaviour of our models, adding rotations also increases the sampling of an orbit. Note as well that each orbit has a counter-rotating sibling, obtained by appropriately changing the sign of the velocity vector.

² Note that the Schwarzschild code by van den Bosch et al. (2008) was developed to model triaxial systems, and therefore also generates initial conditions for box orbits, which have zero time-averaged angular momentum and which can cross the centre (Schwarzschild 1979, 1993). In an axisymmetric potential L_z is conserved and such box orbits will therefore never attain velocities in the azimuthal direction. As this could cause non-axisymmetries in our model we do not specifically generate box orbits.

We further improve the accuracy of the model by ‘dithering’: every orbit is split into N_{dither}^3 suborbits by replacing each of its three nonzero initial coordinates by N_{dither} slightly different coordinates. In fact, the initial conditions of all suborbits are found by increasing N_{ener} , N_{I_2} , and N_{I_3} by a factor of N_{dither} . The observables of each set of adjacent N_{dither}^3 suborbits are combined and stored as being the observables of the (bundled) orbit. Choosing an odd number for N_{dither} ensures that the original orbit is the central suborbit of the bundle. In all our Schwarzschild models we use $N_{\text{dither}} = 5$. Every main orbit is thus made from a bundle of $5^3 = 125$ neighbouring suborbits.

We use a Runge Kutta integrator to compute the stellar trajectories over roughly 200 orbital time scales. We require that the energy of each suborbit is always conserved better than 1% by increasing the accuracy of the integrator if necessary. For each orbit the kinematic information is stored in a velocity grid, which consists of a line-of-sight velocity axis (N_v velocity bins) and an axis associated to the location on the sky (N_{kin} kinematic-bins). On equally spaced time intervals, a count is added to the element of the grid associated to the velocity and location at the given time. The sky projected path of the orbit is determined in a similar way and stored in the surface brightness grid containing $N_{2\text{D light}}$ light-bins. In an additional 3D grid containing $N_{3\text{D light}} = 800$ bins (40 radial, 5 azimuthal and 4 polar bins in the positive octant) the 3-dimensional path of an orbit is stored. This 3D grid reaches radii well beyond the FOV (in contrast to the velocity and surface brightness grid), and is used to control the system at such radii.

In this work we set $N_{2\text{D light}}$ equal to $99 \times 99 = 9801$ and N_{kin} to $9 \times 9 = 81$, unless stated otherwise. The velocity axis of the velocity grid contains $N_v = 41$ bins and has a total velocity width of 80 km/s, such that we cover velocities up to $\pm 4\sigma_E$. The central velocity bin is centred on 0 km/s. To be able to track how long an orbit spends in a given kinematic-bin, counts will also be added to the first or last velocity bin if velocities are beyond the limits of the velocity grid³.

3.2. Fitting orbital weights

Once the orbit libraries are in place, we find the orbital weights such that the total luminous mass, the surface brightness profile and the kinematics within the FOV, and the 3D light profile of the system are reproduced.

The 2D light profile is fitted using the surface brightness grid, where we define:

$$m_j^{\text{light}} = \sum_{i=1}^{N_{\text{orb}}} w_i m_{ij}^{\text{light}}, \quad (5)$$

where we sum over all orbits i . Here, m_{ij}^{light} is the fraction of time orbit i spent in light-bin j and m_j^{light} is the fractional surface brightness in light-bin j . The orbital weights are denoted by w_i

³ When taking too few (i.e. too wide) velocity bins for the velocity grid, the velocity moments might not be recovered correctly. We have also checked that if we bin the true Gaussian line-of-sight velocity profile of our mock galaxy as described above, thus discarding the contribution of velocities that are outside the range of the grid, the velocity moments are recovered well, i.e. the first and third moments are not affected, while the second and fourth velocity moments might result in relative errors of order 0.1% and 2% given the choices made for binning the velocity data.

and add to unity by construction. The 3D light profile is fitted similarly using the 3D grid.

At the same time as we fit the light, we also fit the kinematics. In every kinematic-bin k we compute the first 4 mass-weighted velocity moments $\langle v_k^n \rangle$ by defining:

$$m_k^{\text{kin}} \langle v_k^n \rangle = \sum_{i=1}^{N_{\text{orb}}} w_i m_{ik}^{\text{kin}} \langle v_{ik}^n \rangle, \quad (6)$$

where again we sum over all orbits i . This time m_{ik}^{kin} is the fraction of time orbit i spent in kinematic-bin k and m_k^{kin} is the fractional surface brightness in kinematic-bin k . The n^{th} moment of orbit i in kinematic-bin k is given by $\langle v_{ik}^n \rangle$:

$$\langle v_{ik}^n \rangle = \frac{\sum_{l=2}^{N_v-1} h_{ikl} v_{\text{cen},l}^n \Delta v}{\sum_{l=2}^{N_v-1} h_{ikl} \Delta v}, \quad (7)$$

where, Δv is the size of the velocity bin and h_{ikl} is the fraction of time that orbit i spent in kinematic-bin k and velocity bin l . Velocity bin l has velocity range $[v_{\text{cen},l} - \frac{1}{2}\Delta v, v_{\text{cen},l} + \frac{1}{2}\Delta v]$, where $v_{\text{cen},l}$ denotes its central velocity. We sum over the N_v velocity bins, although we discard the contributions of the first and last velocity bin. This is done since we did not set a stringent outer velocity boundary in these velocity bins: as described before, counts will be added here even if a star has a velocity outside the range of the grid and therefore the typical velocities of these bins are not known. Note that $m_{ik}^{\text{kin}} = \sum_{l=1}^{N_v} h_{ikl}$ with this choice.

Now that we have defined the relation between the observables and the quantities in our model, we can describe how we fit the orbital weights. The fit is based on minimising χ_{tot}^2 :

$$\chi_{\text{tot}}^2 = \sum_{u=1}^{N_{\text{obs}}} \left[\frac{\text{Model}[u] - \text{Data}[u]}{\text{Error}[u]} \right]^2, \quad (8)$$

where u runs over all N_{obs} observables. The number of observables is given by:

$$N_{\text{obs}} = 1 + N_{2\text{D light}} + N_{3\text{D light}} + 4N_{\text{kin}}, \quad (9)$$

which includes the contribution of the total light of the system, the fractional light for each 2D and 3D light-bin, and the four velocity moments for each kinematic-bin, respectively. Since using higher order moments might reduce the degeneracy between the velocity anisotropy and the mass profile (e.g. Merrifield & Kent 1990; Richardson & Fairbairn 2013) we choose to use four velocity moments. We do not use higher moments since these are observationally harder to constrain.

We use a non-negative least square solver to ensure that all orbital weights are positive. The light is weighted by assigning an error of 2% to each of the 2D and 3D light-bins.

We note that we can investigate the individual contribution to the total χ_{tot}^2 by decomposing it, e.g:

$$\chi_{\text{tot}}^2 = \chi_{\text{total light}}^2 + \chi_{2\text{D light}}^2 + \chi_{3\text{D light}}^2 + \chi_{\text{kin}}^2. \quad (10)$$

We stress that χ_{tot}^2 is being minimised. We do not minimise the terms on the right-hand side individually. The term associated to the total light of the system turns out to be negligible, since it is

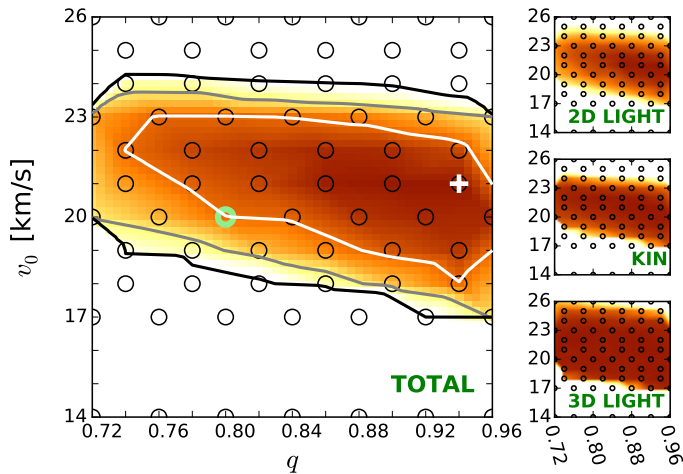


Fig. 2. $\Delta\chi^2$ -distribution of the characteristic parameters q and v_0 of the Evans models obtained after applying the Schwarzschild method. In this case our mock data consist of 10^5 stars inside the FOV (3×3 kpc). We use 9×9 kinematic-bins and assume the potential functional form and inclination are known. The black circles show the locations where the Schwarzschild models were evaluated. The green circle indicates the input parameters of the mock system. The best-fit model is indicated by the white cross and recovers the mock galaxy mass parameter. In white, grey and black we show the $\Delta\chi^2 = [2.3, 6.18, 11.8]$ -contours respectively. The coloured landscape shows interpolated $\Delta\chi^2$ -values, and goes up to a maximum of $\Delta\chi^2 = 10$. On the right we show the $\Delta\chi^2$ -landscapes when only considering $\chi_{2D \text{ light}}^2$ (top), χ_{kin}^2 (middle), or $\chi_{3D \text{ light}}^2$ (bottom).

always recovered very well. The same holds for $\chi_{3D \text{ light}}^2$. These terms are only added to Eq. 8 to ensure that the model returns a realistic galaxy (in the sense that the luminous component might resemble a galaxy). Most of the constraining power thus comes from the surface brightness profile and the kinematics.

4. Results

In this section we show that the Schwarzschild method can recover some of the characteristic parameters of the mock Sculptor-like dwarf spheroidal galaxy. We first show in Sect. 4.1 that if the true potential functional form of the system is known, we can constrain the characteristic mass parameter of the mock galaxy. In reality however, the true potential functional form is not known. Therefore, in Sect. 4.2 we demonstrate how well we can constrain the characteristic parameters when assuming an axisymmetric form of a Navarro-Frenk-White (NFW, Navarro et al. 1996) potential.

4.1. Two parameter Evans models: recovering the mock galaxy parameters

Here we assume the true form of the potential is known, i.e. we use it to build the orbit libraries for the Schwarzschild models. Our aim is to establish whether we can recover the correct values of the characteristic input parameters with this method. To this end we make a grid of models in which we vary the values of the characteristic parameters q and v_0 (see Eq. 1). We thus fix the core radius to $R_c = 1$ kpc, i.e. to its true value. We sample q from 0.72 to 0.96, and v_0 from 11 km/s to 29 km/s, with higher sampling (decided iteratively) having steps in q of 0.02 and in v_0 of 1 km/s. We name the models by the values of their parameters:

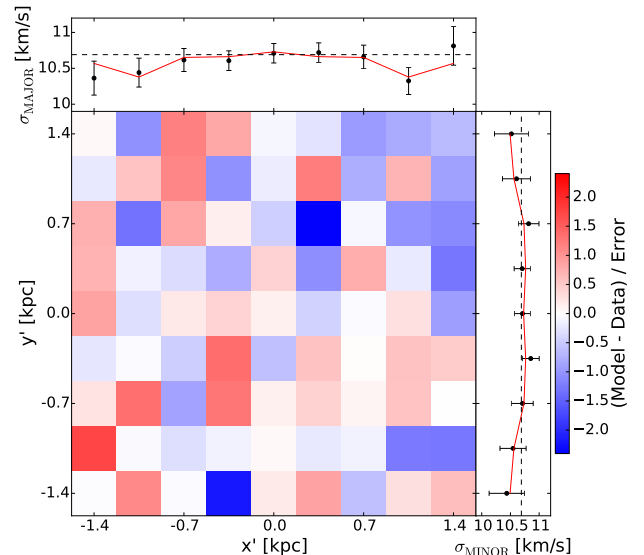


Fig. 3. The difference of the best fit and the observed velocity dispersion in terms of the observed error, for all 9×9 kinematic-bins. The figure is obtained after fitting the q94v21 library to our mock data consisting of 10^5 stars in our FOV, assuming an edge-on view. The top and the right panels show the fit (red full line) obtained along the major and minor axis respectively. The data points with 68% error bars are shown in black. Black dashed lines indicate the true velocity dispersions from theory (Eq. 4).

qXXvYY in which $XX = 100q$ and $YY = v_0$ in km/s. For the orbit sampling, we set $N_{\text{ener}} = 32$, $N_{l_2} = 32$ and $N_{l_3} = 16$ such that a total of $32 \times 32 \times 16 \times 5^3 = 2048000$ suborbits are integrated (see Sect. 3.1) and $2 \times 32 \times 32 \times 16 = 32768$ orbital weights are determined (see Sect. 3.2).

4.1.1. Results for a large sample

We start with an idealised case in which the data consist of 10^5 stars. For 9×9 kinematic-bins on the sky, the typical error of the velocity dispersion in a kinematic-bin is ~ 0.25 km/s.

The large panel of Fig. 2 shows the results obtained by fitting the Schwarzschild models to the data. The small black circles show the grid of tested values for q and v_0 , the green circle the true input values, and the white cross indicates the values of the parameters corresponding to the maximum likelihood estimator (MLE). For the best-fit model q94v21 we find $\chi_{\text{tot}}^2 = 207.7$. The contribution of the kinematics (see Eq. 8) to this value is 205.6. Using 81 kinematic-bins to fit 4 velocity moments, this corresponds to 0.64 per kinematic constraint.

We have computed $\Delta\chi^2(q, v_0) = \chi_{\text{tot}}^2(q, v_0) - \min[\chi_{\text{tot}}^2]$ for each of these models and define 68%, 95% and 99.7% - confidence intervals (white, grey and black contours, respectively) at $\Delta\chi^2 = [2.3, 6.18, 11.8]$ (Press et al. 1992)⁴. The coloured background shows the $\Delta\chi^2$ -landscape and is truncated at $\Delta\chi^2 = 10$. The smaller panels on the right show the $\Delta\chi^2$ -landscapes when only considering $\chi_{2D \text{ light}}^2$ (top), χ_{kin}^2 (middle), or $\chi_{3D \text{ light}}^2$ (bottom). The $\Delta\chi^2$ -landscape based on χ_{tot}^2 is thus slightly dominated by the differences in $\chi_{2D \text{ light}}^2$, although the kinematics provide similar constraints.

To estimate the error on the mass parameter we first marginalize over the flattening parameter by selecting for each

⁴ We used the `scipy.interpolate.LinearNDInterpolator` to interpolate the $\Delta\chi^2$.

v_0 the minimum $\Delta\chi^2$ along q . We define the 68% error at those values where $\Delta\chi^2 = 1.0$ (Press et al. 1992). For this experiment we find $v_0 = 21^{+1.33}_{-2.11}$ km/s. We therefore conclude that we can recover the input mass parameter of our mock galaxy well, but as Figure 2 shows we do not constrain well the flattening q .

In Fig. 3 we show how well the velocity dispersion is fitted in the best-fit q94v21 model. For each kinematic-bin, we show how much the model deviates from the data expressed in units of the error on the data. On top we show the fit along the major axis while the subpanel on the right shows the fit along the minor axis. These figures show that the fit is very good (and in fact, it is almost indistinguishable from the fit obtained for what would be the input parameters model, i.e. q80v20).

4.1.2. Downsampling and folding data

We now consider the more realistic case of a sample of 10^4 stars. To reduce the observed uncertainties on the kinematics we decided to fold the kinematic data (but not the light). Since the system is axisymmetric, we fold our data into the kinematic-bins located in the first quadrant. We can simply move each star towards its corresponding kinematic-bin without changing its velocity, because our system has an identical Gaussian line-of-sight profile everywhere (see Sect. 2.1). In general, however, one should change the velocities following the assumed symmetry.

Since we fold the data from 9x9 bins of our FOV into the first quadrant, we effectively have 10^4 stars located in the resulting 5x5 kinematic-bins. A typical kinematic-bin now contains 400 stars on average, and the typical error on the velocity dispersion is ~ 0.45 km/s.

We fit the folded data with the Schwarzschild orbit superposition method and find the MLE for model q90v22 (see Fig. 4). As in the case of 10^5 stars, and thus as expected, the flattening parameter remains fairly unconstrained. We find a slightly larger mass parameter $v_0 = 22^{+1.02}_{-1.44}$ km/s, but $v_0 = 20$ km/s is still within the 95%-confidence region.

For the best-fit model q90v22 we find $\chi^2_{\text{tot}} = 16.5$. The contribution of the kinematics (see Eq. 8) to this value is 13.2. Both values are much lower than in the case of 10^5 stars, and this can be explained by the decrease in the number of kinematic constraints and the fact that the data have now been folded.

It is encouraging that a more realistic number of stars still gives such tight constraints. Comparing the 10^4 stars folded case to the case of 10^5 stars, the 2D 68%-probability contours are shifted towards just slightly larger masses. Note that the uncertainty on the mass parameter did not increase.

To further test how the results depend on the number of stars observed, we decreased even further the number of stars to a sample of 2000 stars. This is the typical size of currently available datasets used to put constraints on the mass of dSph galaxies (e.g. Walker et al. 2009b; Breddels & Helmi 2013; Hayashi & Chiba 2015). We again fold the data from 9x9 into 5x5 kinematic-bins. The resulting typical error on the velocity dispersion in a kinematic-bin is then ~ 0.9 km/s. In this case we find a best-fit model q92v23 ($\chi^2_{\text{tot}} = 38.9$, $\chi^2_{\text{kin}} = 32.6$). The $\Delta\chi^2$ -distribution is shown in Fig. 5. The best models are again reproduced by the most round models, although statistically the flattening parameter remains unconstrained. The region spanned by the contour drawn at $\Delta\chi^2 = 11.8$ is of similar size, but is shifted towards slightly higher masses ($\Delta v_0 \sim 1$ km/s) in comparison to the case of 10^4 stars. The true q80v20 model is nevertheless still within the inferred 99.7%-confidence interval.

The weak trend found for smaller samples to prefer slightly higher values of v_0 may be due to the fact that, for small radii

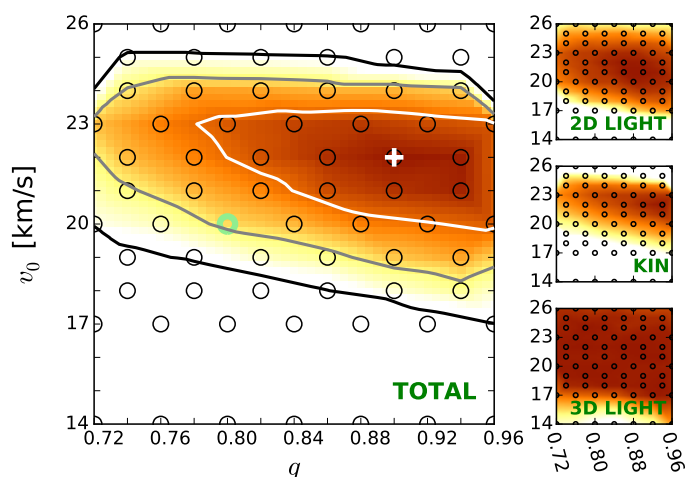


Fig. 4. Similar to Fig. 2, but now using 10^4 stars and using the approach of folding the data from 9x9 into 5x5 kinematic-bins. The parameter inferences are similar, though slightly larger masses are preferred.

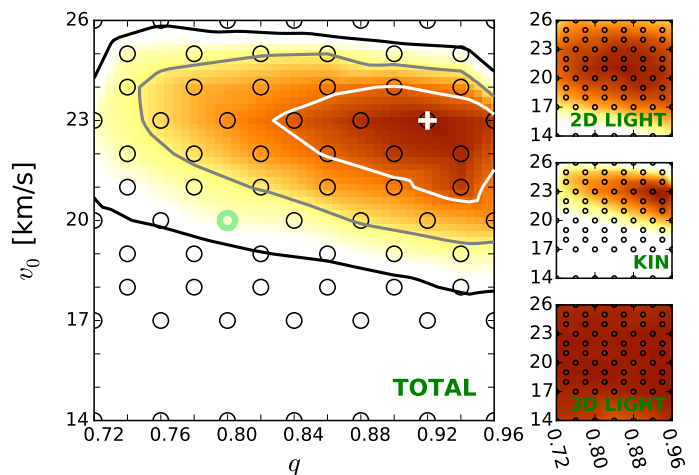


Fig. 5. Similar to Fig. 4, now using 2000 stars. The parameter inferences are similar, though slightly larger masses are inferred ($\Delta v_0 \sim 1$ km/s).

(compared to R_c), the potential (see Eq. 1) is proportional to $v_0^2 [\ln R_c^2 + (R/R_c)^2] + (v_0/q)^2 (z/R_c)^2$. Therefore, there is a weak degeneracy in the term v_0/q , that may manifest itself more when the sampling is sparse, and thus lead to a small shift in preferred values of v_0 for larger q .

From the tests performed in this Section we conclude that, with a kinematic sampling that follows the light, we can not aim to constrain the flattening of an *isothermal* dSph galaxy⁵, even if the true functional form of the potential is known. This is likely because the information content in a velocity dispersion regarding the geometric shape of the potential is too small (since σ is constant across the whole system). We can however still reliably constrain the mass parameter of such a system, i.e. even though the true flattening remains unknown. This can already be done for a realistic number of stars.

⁵ Slightly better results can be obtained by sampling uniformly with distance, see Appendix B.

4.2. Axisymmetric NFW models

We have shown that the Schwarzschild method can constrain correctly the mass parameter when the true functional form of the potential is known. Now, we will tackle the problem more realistically by allowing a different functional form for the potential. We consider an axisymmetric NFW-profile, and follow the parametrization of Vogelsberger et al. (2008):

$$\Phi_V(\tilde{r}) = -4\pi G\rho_0 R_s^3 \left[\frac{\ln(1 + \tilde{r}/R_s)}{\tilde{r}} \right], \quad (11)$$

where R_s is the scale radius and ρ_0 a characteristic density parameter. In comparison to the spherical NFW-profile, the radius $r = \sqrt{R^2 + z^2}$ is replaced by a newly defined radius:

$$\tilde{r} = \frac{(r_a + r)r_E}{r_a + r_E}, \quad (12)$$

where, for the axisymmetric case, $r_E = \sqrt{\left(\frac{R}{a}\right)^2 + \left(\frac{z}{c}\right)^2}$ is the ellipsoidal radius with a and c specifying the relative lengths of the major and minor axes, and where r_a is a transition radius. In addition, we require that $2a^2 + c^2 = 3$, such that when $a = c = 1$, this results in the spherical NFW profile. For $r \gg r_a$, $\tilde{r} \rightarrow r$, whereas for $r \ll r_a$, $\tilde{r} \rightarrow r_E$. Therefore, the gravitational potential is axisymmetric in the central regions and becomes spherical in the outer regions. We set the transition radius to $r_a = 10$ kpc. In all our Vogelsberger models we keep the transition radius r_a fixed.

To additionally guarantee that the total mass density is positive up to at least the orbits possessing the highest energies in our library (~ 50 kpc), the flattening parameter must satisfy $c/a \gtrsim 0.7$ for a case with $R_s = 1$ kpc. For smaller scale radii, larger lower limit values of c/a are needed to satisfy the positive density criterion.

For convenience, we define a characteristic mass parameter, $M_{1\text{kpc}}$ expressed in units of M_\odot , which corresponds to the total enclosed mass within 1 kpc from the centre for a spherical NFW profile with scale radius R_s , i.e.

$$M_{\text{NFW}}(r = 1\text{kpc} | R_s) = 4\pi\rho_0 R_s^3 \left[\ln\left(\frac{R_s + r}{R_s}\right) - \left(\frac{r}{R_s + r}\right) \right]_{1\text{kpc}}. \quad (13)$$

From this equation we determine the value of ρ_0 , and it is this value of ρ_0 that we use for the axisymmetric Vogelsberger potential in Eq. 11.

4.2.1. The ‘true’ (equivalent) Vogelsberger system

Before we can test the Schwarzschild orbit superposition method while assuming Vogelsberger mass models, we need to know when a result can be considered satisfactory. Since we could not constrain the flattening for the case when the true potential form is known we will not aim to constrain the flattening for the Vogelsberger models. Nevertheless, the expected best-fit scale radius R_s and mass $M_{1\text{kpc}}$ of our system will depend on the c/a -value assumed. In this section we therefore establish what are good parameters for the mass $M_{1\text{kpc}}$, scale radius R_s , and flattening c/a , such that the properties of the Evans mock galaxy are reproduced the best.

Because most stars of our mock galaxy will have projected radii in between 0.5 and 2.0 kpc from the centre, we require that the flattening of the Vogelsberger potential should be comparable

to that of the mock galaxy over this region. At a given position we define the Vogelsberger potential flattening q_V as the axis ratio of the equipotential contour that goes through that point. For a position (R, z) , we thus define $q_V(R, z) = z_\phi/R_\phi$, where $\Phi(R = 0, z_\phi) \equiv \Phi(R_\phi, z = 0) \equiv \Phi(R, z)$. On such equipotential, it must hold that $\tilde{r}(R = 0, z_\phi) = \tilde{r}(R_\phi, z = 0)$, and since \tilde{r} only depends on c/a , $q_V(R, z)$ is independent of our mass parameter and scale radius⁶. We take values for z_ϕ from 0.5 to 2.0 kpc in steps of 0.05 kpc along the minor axis and compute the corresponding R_ϕ -values (i.e. the radii where the equipotential contours that belong to z_ϕ cross the major axis). For a given c/a we then compute the mean of the absolute differences between the Evans mock galaxy potential flattening ($q = 0.8$) and the Vogelsberger potential flattening along the defined range for z_ϕ , i.e. we compute: $\text{mean}(|q - q_V(R = 0, z_\phi)|)$. We find that for $c/a \simeq 0.776$ this average difference is smallest (see left panel of Fig. 6). For our range of z_ϕ and $c/a = 0.776$, the Vogelsberger potential flattening increases almost linearly with z_ϕ , though the gradient is small (0.018 kpc^{-1}).

Given this value for the flattening, we proceed to obtain the best equivalent values for the mass and scale radius of the mock galaxy now described by the Vogelsberger profile. We do this by comparing $|RF_R| \equiv \sqrt{R} \left| \frac{\partial}{\partial R} \Phi(R, z = 0) \right|$ along the major axis and $|zF_z| \equiv \sqrt{z} \left| \frac{\partial}{\partial z} \Phi(R = 0, z) \right|$ along the minor axis with respect to their values for the mock Galaxy. We investigate their trends for R - and z -values identical to those used for z_ϕ previously.

We vary the scale radius and the mass parameter $\log_{10}(M_{1\text{kpc}}[M_\odot])$ and compute the mean of the absolute differences with respect to the mock galaxy obtained along the major and minor axis for $c/a = 0.776$. We denote this by $\langle \Delta v \rangle := \text{mean}[0.5\{\text{abs}(\Delta|RF_R|) + \text{abs}(\Delta|zF_z|)\}]$. From the right panel of Fig. 6 we infer that $\langle \Delta v \rangle$ is minimum for mass parameter $\log_{10}(M_{1\text{kpc}}[M_\odot]) \simeq 7.69$ and scale radius $R_s = 4.9$ kpc (green circle), although any value with $R_s \geq 2$ kpc works well, as $\langle \Delta v \rangle$ does not vary strongly. To be able to compare these findings to the results from our Schwarzschild models (see Sect. 4.2.2), we estimate the error on these ‘true’ parameters by considering those locations where $\langle \Delta v \rangle$ changes by a factor 2 with respect to its minimum value (green contour). The mass parameter is then within the range $[7.63, 7.73]$, the scale radius larger than 2.4 kpc. For the smaller scale radii ($R_s < 2$ kpc) slightly higher values for the characteristic mass parameter would be preferred, but $\langle \Delta v \rangle$ is also larger in such cases. Note that the NFW mass value that we just estimated corresponds well to the mass enclosed within 1 kpc of a spherical Evans model with $R_c = 1$ kpc and $v_0 = 20$ km/s (as assumed in Sect. 2), since then $\log_{10}(M_{1\text{kpc,Evans}}[M_\odot]) \simeq 7.67$.

Although we will not constrain the flattening of the system, we can investigate how the expected best-fit parameters change if different values for c/a are taken. Setting $c/a = 0.70$ results in $\langle \Delta v \rangle = 0.32$ km/s for its minimum at $\log_{10}(M_{1\text{kpc}}[M_\odot]) \simeq 7.69$ and $R_s = 4.4$ kpc, and setting $c/a = 0.85$ results in $\langle \Delta v \rangle = 0.37$ km/s for $\log_{10}(M_{1\text{kpc}}[M_\odot]) \simeq 7.69$ and $R_s = 5.1$ kpc. The expected best-fit mass parameter is thus not affected by the choice of c/a . The expected best-fit scale radius only increases slightly for larger values for the flattening parameter (i.e. rounder shapes), though the effect⁷ is rather small. In addition, the grey

⁶ More precisely, \tilde{r} depends on r_a and $r_E(c/a)$, but we have chosen to fix the value of r_a (and make it independent of R_s).

⁷ Even for a spherical potential, i.e. $c/a = 1.0$, we find the minimum $\langle \Delta v \rangle = 0.62$ km/s to be located at $\log_{10}(M_{1\text{kpc}}[M_\odot]) \simeq 7.68$ and $R_s = 6.1$ kpc.

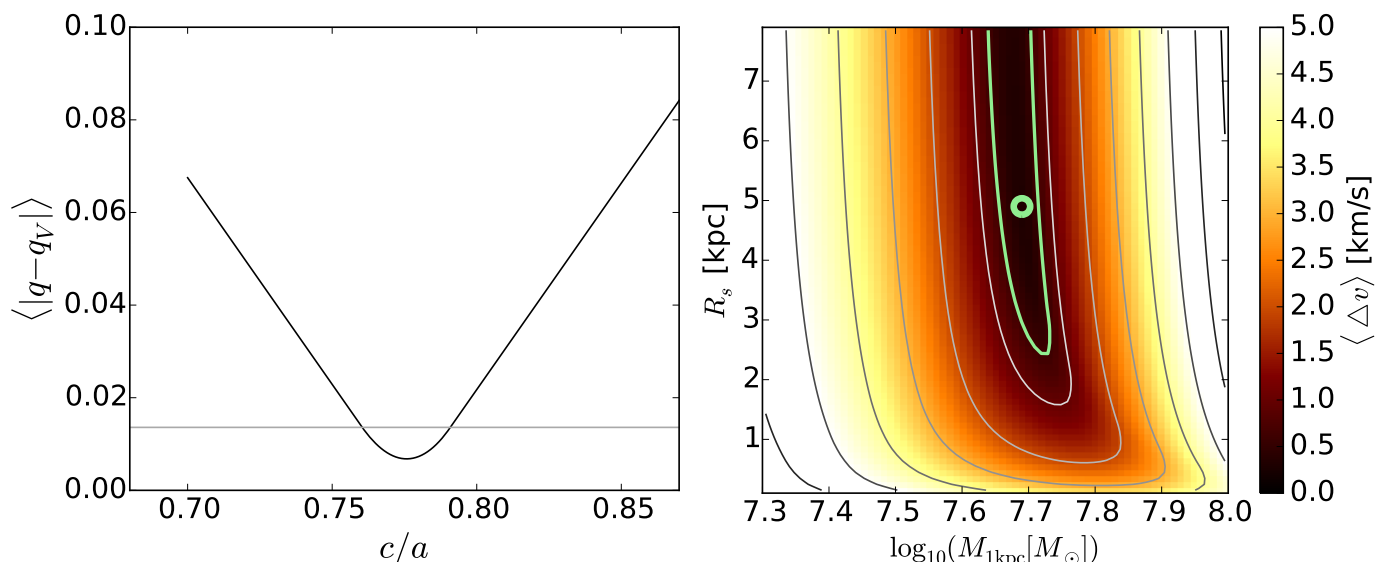


Fig. 6. Estimating the ‘true’ parameters of the Vogelsberger system by comparing the differences in potential flattening on the left and the differences in the gradients of the potentials on the right. The comparisons are based on the distance interval from 0.5 up to 2.0 kpc (with steps of 0.05 kpc) from the centre of the galaxy. Left: The mean absolute difference of the Vogelsberger potential flattening and the true potential flattening of the mock galaxy as a function of the flattening parameter c/a of the Vogelsberger potential (black line). The grey horizontal line marks the positions where this difference has doubled, with respect to the minimum 0.007 at $c/a \approx 0.776$. Right: We minimise the mean of the absolute differences in the gradients of the potential along the major and minor axis (compared to the mock galaxy) by varying the Vogelsberger model parameters $M_{1\text{kpc}}$ and R_s . The figure is obtained after setting the flattening parameter to $c/a = 0.776$. The colour bar is truncated at 5.0 km/s. The green circle indicates the location at $\log_{10}(M_{1\text{kpc}}[M_{\odot}]) \approx 7.69$ and $R_s = 4.9$ kpc where the differences are minimum ($\langle \Delta v \rangle_{\min} = 0.31$ km/s). Grey lines indicate the contours of constant mean absolute differences and are spaced by 1 km/s. As a proxy for the error on the Vogelsberger parameters, a green contour is drawn where the differences are doubled with respect to the minimum difference.

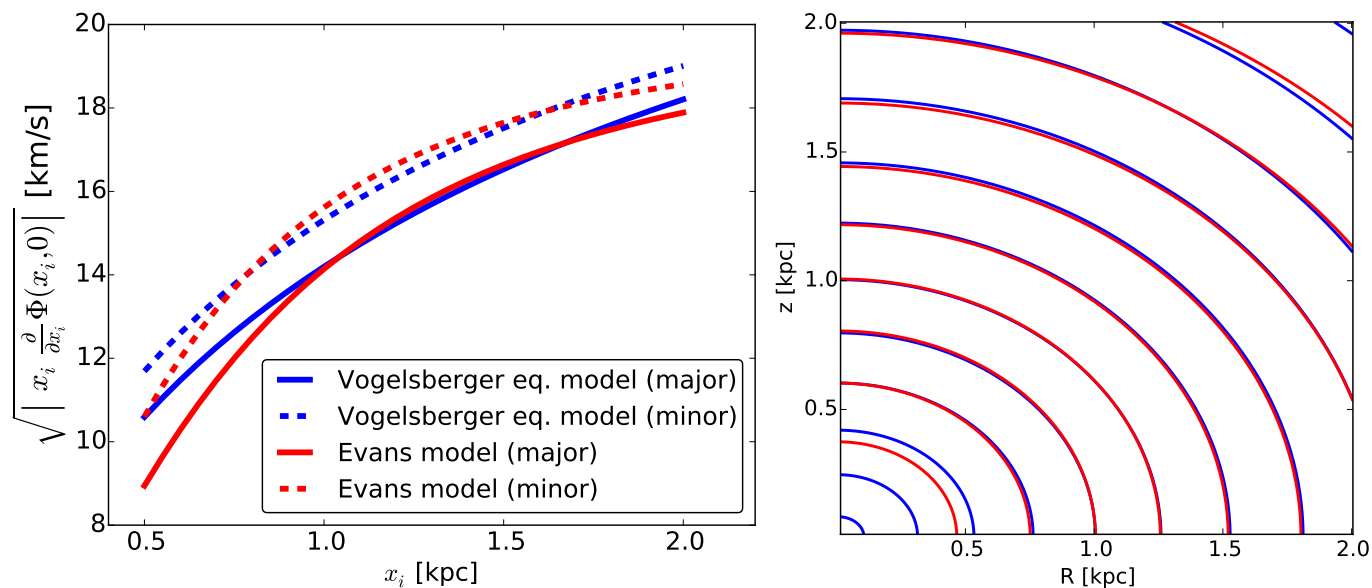


Fig. 7. Left: The major (full lines) and minor (dashed lines) axis gradients of the potential as function of R and z respectively for the true Evans model (red) and for the ‘equivalent’ Vogelsberger potential with $c/a \approx 0.776$, $R_s \approx 4.9$ kpc and $\log_{10}(M_{1\text{kpc}}[M_{\odot}]) \approx 7.69$ (blue). Right: Comparison of the isopotential contours for the true Evans (red) and the equivalent Vogelsberger models (blue). For the purpose of this figure the zero-point of the potential is chosen here such that $\Phi_E = \Phi_V$ at $(R, z) = (1, 0)$ kpc. For each potential, contours are drawn at the positions where Φ has changed in steps of $50 \text{ km}^2/\text{s}^2$. In the region from 0.7 up to 2 kpc the equivalent Vogelsberger model follows well the true Evans potential. For more inner radii the (cusped) Vogelsberger models can not reproduce the (less steep) cored behaviour of the Evans potential.

contours, which are drawn at fixed $\langle \Delta v \rangle$, span very similar regions for different values for c/a .

In Fig. 7 we compare the Vogelsberger equivalent potential to the true Evans potential of our galaxy. In the left panel we show the gradients of the potentials along the major and minor

axis. Note that the Evans model seems to have lower $|RF_R|$ and $|zF_z|$ for $R \lesssim 1$ kpc and $z \lesssim 0.75$ kpc, respectively, than the NFW ‘equivalent’ model. In the panel on the right we confirm that the potential flattening is matched quite well by showing isopotential contours. Both panels reveal that only in the centre

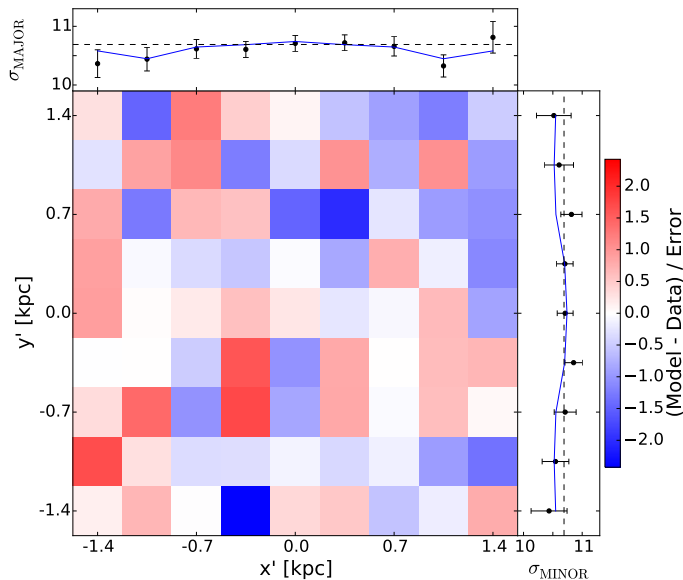


Fig. 8. Difference between the best fit Vogelsberger model (M772Rs250, blue line in the subpanels) and the observed velocity dispersion when applying the Schwarzschild method in 9x9 kinematic-bins to our mock dataset consisting of 10^5 stars in the FOV (see Fig. 3 for a comparison).

(< 0.7 kpc) and at the distances larger than 3 kpc, the gradients of both potentials start to deviate from each other.

In summary, the equivalent Vogelsberger system can be described by $\log_{10}(M_{1\text{kpc}}[M_{\odot}]) \simeq 7.69^{+0.04}_{-0.06}$ and by $R_s \gtrsim 2.4$ kpc (with its most likely value at $R_s = 4.9$ kpc) for $c/a = 0.776$.

4.2.2. Fitting Vogelsberger models with the Schwarzschild method: exploring different sample sizes

Since we could not constrain the flattening parameter when the potential functional form was known (see Sect 4.1), we can not expect to constrain the flattening if we examine a different functional form. We set $c/a = 0.80$, equal the observed flattening in the light, and subsequently find the inferences on the mass and scale radius. We initially make a grid in $(\log_{10}(M_{1\text{kpc}}), R_s)$ -space, where R_s ranges from 1 to 8 kpc with steps of $\Delta R_s = 1$ kpc, while for the characteristic mass we take steps of 0.05 for values from $\log_{10}(M_{1\text{kpc}}[M_{\odot}]) = 7.55$ to $\log_{10}(M_{1\text{kpc}}[M_{\odot}]) = 7.85$, i.e. just spanning a factor of 2 in mass. Later, we also decided to sample $\log_{10}(M_{1\text{kpc}}[M_{\odot}]) = [7.68, 7.72]$ for $R_s \in [1.5, 7.5]$ kpc with a similar ΔR_s step.

To be more efficient we decrease the number of orbits compared to Sect. 4.1 and set $N_{\text{ener}} = 24$, $N_{I_2} = 24$ and $N_{I_3} = 8$, such that a total of $24 \times 24 \times 8 \times 5^3 = 576000$ suborbits are integrated and $2 \times 24 \times 24 \times 8 = 9216$ orbital weights are determined. We have found this gives good results in terms of recovery of the light profile and kinematics. In addition we also add regularisation terms to the fit in this more realistic experiment: by applying regularisation we set additional constraints such that the orbital weights are more smoothly distributed, i.e. in a more physical way (as the weights relate to the distribution function, which itself is expected to be smooth). More details on the concept of regularisation and its effects can be found in Appendix C.

We present the results following the same structure of Sect. 4.1 and name the Vogelsberger models by MxxxRyyyy, where xxx = $100 \log_{10}(M_{1\text{kpc}}[M_{\odot}])$ and yyy = $100R_s$ (in kpc). We discuss how well we can recover the characteristic parameters of

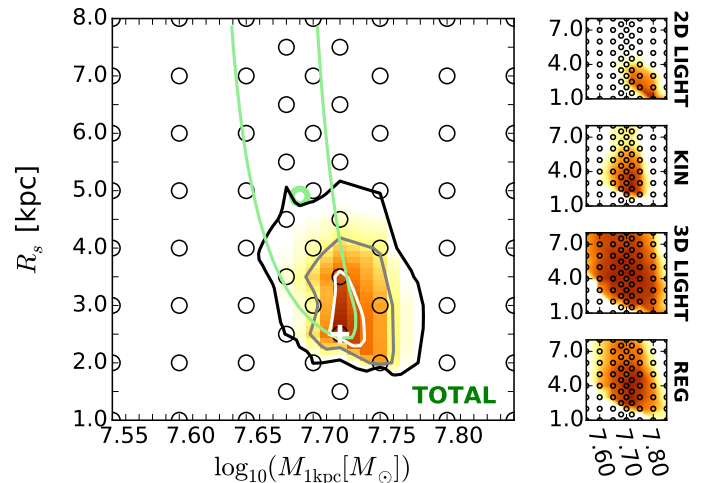


Fig. 9. Confidence intervals for the axisymmetric Vogelsberger model in $(\log_{10}(M_{1\text{kpc}}), R_s)$ (after fixing $c/a = 0.8$) for the dataset with 10^5 stars and 9x9 kinematic-bins. The $\Delta\chi^2 = [2.3, 6.18, 11.8]$ -contours are in white, grey and black respectively. The best-fit model is indicated by the white cross, while the expectations are given by the green contour (identical to that shown in Fig. 6). The mass parameter is well constrained and models with $R_s \leq 2.0$ kpc are strongly disfavoured, consistent with our expectations. The small panels on the right show the $\Delta\chi^2$ -landscapes when only considering $\chi^2_{2\text{D light}}$ (top), χ^2_{kin} (top-middle), $\chi^2_{3\text{D light}}$ (bottom-middle), or χ^2_{reg} (bottom).

the Vogelsberger potential for mock datasets containing 10^5 , 10^4 and 2000 stars.

We start with the case of 10^5 stars for which we use 9x9 kinematic-bins and no folding. For this case, we find that model M772Rs250 provides the best fit ($\chi^2_{\text{tot}} = 275.1$). Fig. 8 shows that this model reproduces well the mock velocity dispersions in all kinematic-bins (since $\chi^2_{\text{kin}} = 220.9$, which results in 0.68 per kinematic constraint). The fit is of comparable quality to the best-fit Evans model (for the same case) although the light is recovered slightly less well, which may be driven by the smaller number of orbits being used now.

Fig. 9 shows the resulting $\Delta\chi^2$ -distribution in $(\log_{10}(M_{1\text{kpc}}), R_s)$ -parameter space. The scale radius of the Vogelsberger potential is constrained to $R_s = 2.5^{+0.6}_{-0.1}$ kpc and the mass parameter to $\log_{10}(M_{1\text{kpc}}[M_{\odot}]) = 7.72^{+0.01}_{-0.01}$. The Schwarzschild model thus prefers values towards the lower end for the scale radius and a mass parameter that agrees well with of our expectations. The panels on the right show the $\Delta\chi^2$ -landscapes when only considering $\chi^2_{2\text{D light}}$ (top), χ^2_{kin} (top-middle), $\chi^2_{3\text{D light}}$ (bottom-middle), or χ^2_{reg} (bottom). The total $\Delta\chi^2$ -landscape is dominated by the kinematics and 2D light.

Similar best-fit parameters are obtained for a smaller mock dataset with 10^4 stars when folding the data into 5x5 kinematic-bins, as shown in Fig. 10. The mass and scale parameters are constrained to $R_s = 3.0^{+0.7}_{-0.4}$ kpc and $\log_{10}(M_{1\text{kpc}}[M_{\odot}]) = 7.75^{+0.05}_{-0.03}$. For the best-fit model M775Rs300, $\chi^2_{\text{tot}} = 78.0$ and $\chi^2_{\text{kin}} = 33.9$, or 0.339 per kinematic constraint on average. This χ^2_{tot} is lower than for the case of 10^5 stars, likely because we folded the data. In comparison to the best-fit Evans model, the quality of the fit of the kinematics is slightly worse but still very good.

When decreasing the sample size even further to 2000 stars, we find that models with low values for R_s and larger $\log_{10}(M_{1\text{kpc}}[M_{\odot}])$, are now preferred as shown in Fig. 11, al-

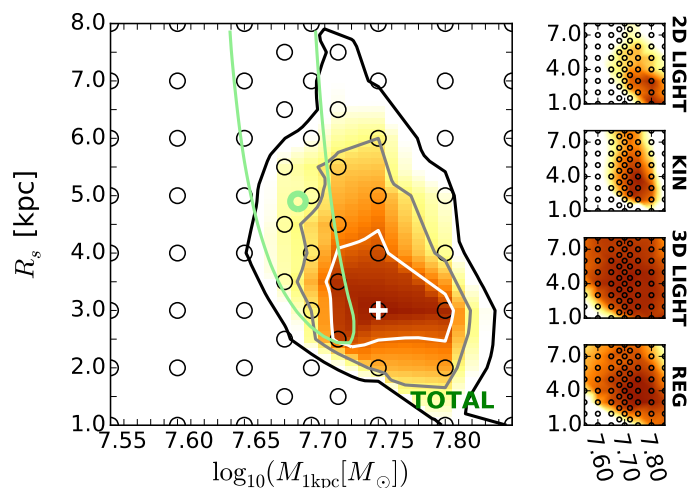


Fig. 10. Similar to Fig. 9, but now after fitting mock data consisting of 10^4 stars and folding into 5×5 kinematic-bins. The decrease in sample size (by a factor 10) has led to a slight increase by the area spanned by the probability contours, although the inference on the mass parameter is still very good and only changed to slightly higher masses.

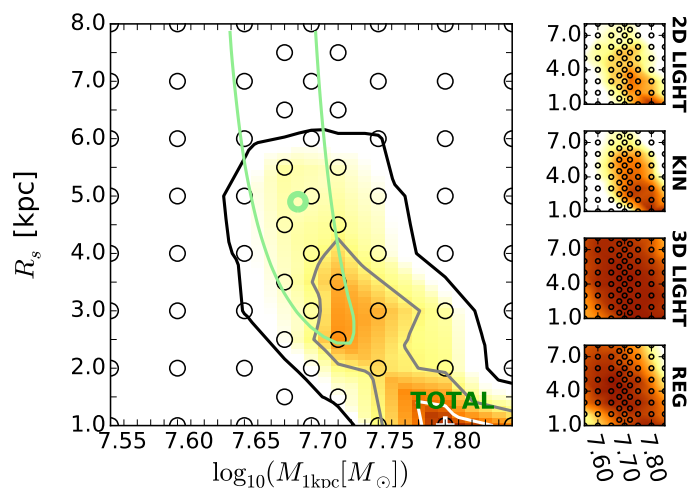


Fig. 11. As in Fig. 10, but now for a dataset with 2000 stars. Note how the confidence contours follow the shape of the green contour (derived in Fig. 6).

though the 95%-confidence region still overlaps with the expected values for the parameters. We obtain best-fit values of $R_s = 1.0^{+0.2}_{-0.0}$ kpc and $\log_{10}(M_{1\text{kpc}}[M_{\odot}]) = 7.80^{+0.02}_{-0.01}$.

It is interesting to note that the shape of the confidence contours obtained from the Schwarzschild method for all sample sizes, follows very closely the shape of the contours of $\langle \Delta v \rangle$ depicted in Fig. 7. Recall that the quantity $\langle \Delta v \rangle$ is a proxy for the difference in enclosed mass between the Evans and Vogelsberger model. This implies that Schwarzschild’s method is actually very sensitive to enclosed mass, and it is identifying the set of Vogelsberger models that best follow the true underlying mass distribution. Also interesting is that the trend favouring larger values of the mass parameter when decreasing sample size, is present both for the Evans as well as for the Vogelsberger models.

We compare the Evans and Vogelsberger best-fit models to the observed velocity dispersions in Fig. 12. The left and right panels compare the behaviour on the major and minor axes respectively, for different sample sizes: 10^5 , 10^4 and 2000 stars (in

the top, middle and bottom rows respectively). The shaded areas enclose the minimum and maximum velocity dispersions for the evaluated models within the $\Delta\chi^2 = [2.3, 6.18, 11.8]$ -contours. These comparisons show that the Evans models fit the kinematics slightly better but that nearly equally good fits are provided by the Vogelsberger models (except in along the minor axis for the smallest dataset, bottom right panel).

From the analyses presented in this section we may thus conclude that the Schwarzschild modelling technique is sensitive to the mass enclosed and that it is successful in constraining well the mass parameter of the models, even if the functional form of the potential is not known.

5. Discussion and Conclusions

We explored the ability of the Schwarzschild’s orbit superposition method to characterise the intrinsic properties of an axisymmetric dSph galaxy, such as its mass, scale radius and flattening. We did this by setting up an isothermal Sculptor-like mock galaxy that is flattened in both the luminous and dark components. We have shown that Schwarzschild’s method applied to mock datasets with a realistic number of stars with measured radial velocities distributed following the luminosity profile of the system, is successful in recovering the characteristic mass parameter of the underlying (true) logarithmic potential, even if the potential flattening is not known. On the other hand, we find that we can not put constraints on the flattening parameter.

Most likely, our inability to constrain the flattening is the consequence of our choice of the specific Evans model for our mock galaxy. In this model with a distribution function that is ergodic, the line-of-sight velocity profile is exactly the same everywhere and depends on the mass parameter only. This means that the kinematics are independent of the inclination and flattening, and the light alone does not contain enough information to constrain the flattening parameter.

One might also argue that it might not be optimal for a spectroscopic survey to sample stars according to the light profile of the system. In fact, slightly better results were obtained when the dataset with radial velocities provided an equal number of stars to each kinematic-bin. All these factors, in combination with the fact that for our specific Evans model just $\sim 30\%$ of the system’s light is within our FOV, are likely playing a role. It might be possible however that better results could be obtained with a more realistic and general distribution function (i.e. non-ergodic), applied to a galaxy for which the kinematic tracers cover well the full system and sample more the outskirts.

Since in reality the potential functional form is not known, we also explored the case in which we assume an axisymmetric NFW model. We first determined the values of the characteristic parameters of the NFW model that mimic the mock galaxy best by comparing some basic properties (potential flattening and gradients in the potential). We found that even in this case, i.e. the orbits that form the building blocks of Schwarzschild’s method are integrated in the wrong potential, we can retrieve the correct characteristic mass and scale parameters.

We have explored the dependencies of our results on the sizes of the data samples used, and find that a decrease in the number of stars with line-of-sight velocities, only slightly affects the determination of the characteristic parameters of the model. For the smallest sample considered, with 2000 stars, the inference on the mass of the NFW “equivalent” model is somewhat poorer but the true value differs by only 20% from the best-fit and also lies within the 95% confidence interval.

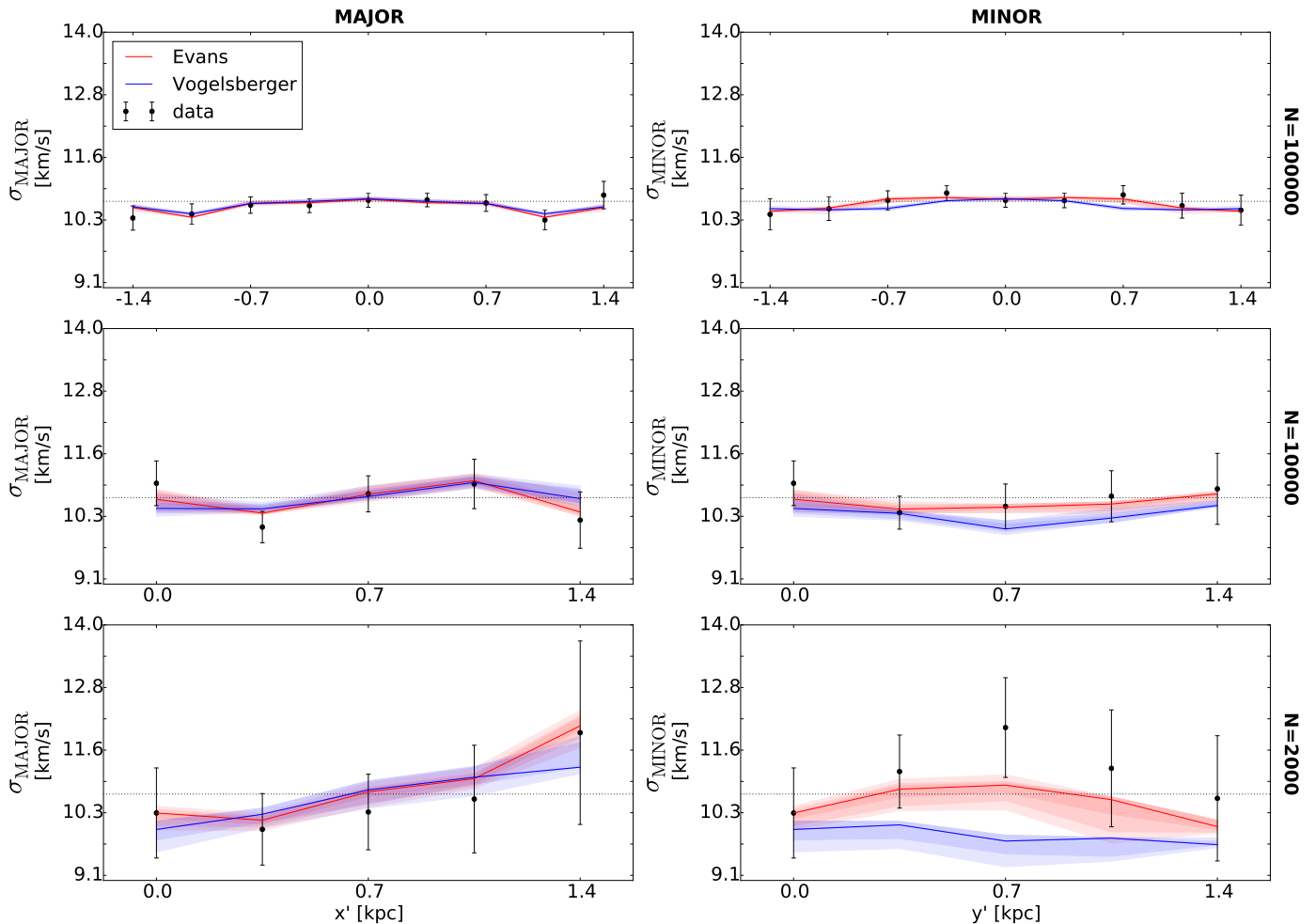


Fig. 12. Comparison of the results from the Schwarzschild modelling fits to the observed velocity dispersion along the major (left column) and minor (right column) axis. From top to bottom we show the best-fit Evans (red line) and Vogelsberger (blue line) models for datasets containing $N = 10^5$, $N = 10^4$, and 2000 stars, respectively. The shaded regions denote the error bands computed as described in the text. Black dotted lines indicate the input (theoretical, Eq. 4) velocity dispersions.

We have checked that our results are not strongly dependent on the choices of e.g. the number of orbits in the orbit libraries, number of kinematic- or light-bins, and the number of velocity bins. Furthermore we have also briefly investigated the distribution functions for the best-fit models, and found that, particularly when regularisation is included, they are quite similar to the distribution function of the mock dwarf spheroidal galaxy.

In conclusion, it is promising that the mass of our flattened system can be recovered so well even if the flattening parameter is unknown. This is also aligned with the results of Kowalczyk et al. (2018), who applied their spherical Schwarzschild models on non-spherical objects. To some extent, this provides us with more confidence regarding previously reported estimates of the mass of dSph galaxies obtained assuming spherical symmetry.

Acknowledgements. We thank R. van den Bosch for supplying us the Schwarzschild code and L. Posti and P.T. de Zeeuw for many useful discussions regarding the project. A.H. acknowledges financial support from a VICI grant from the Netherlands Organisation for Scientific Research, NWO.

References

Battaglia, G., Helmi, A., & Breddels, M. 2013, *New A Rev.*, 57, 52
 Battaglia, G., Helmi, A., Tolstoy, E., et al. 2008a, *ApJ*, 681, L13
 Battaglia, G., Irwin, M., Tolstoy, E., et al. 2008b, *MNRAS*, 383, 183

Battaglia, G., Tolstoy, E., Helmi, A., et al. 2011, *MNRAS*, 411, 1013
 Battaglia, G., Tolstoy, E., Helmi, A., et al. 2006, *A&A*, 459, 423
 Binney, J. & Tremaine, S. 2008, *Galactic Dynamics: Second Edition* (Princeton University Press)
 Boylan-Kolchin, M., Bullock, J. S., & Kaplinghat, M. 2011, *MNRAS*, 415, L40
 Breddels, M. A. & Helmi, A. 2013, *A&A*, 558, A35
 Breddels, M. A., Helmi, A., van den Bosch, R. C. E., van de Ven, G., & Battaglia, G. 2013, *MNRAS*, 433, 3173
 Brooks, A. M., Kuhlen, M., Zolotov, A., & Hooper, D. 2013, *ApJ*, 765, 22
 Evans, N. W. 1993, *MNRAS*, 260, 191
 Evans, N. W., An, J., & Walker, M. G. 2009, *MNRAS*, 393, L50
 Hayashi, K. & Chiba, M. 2012, *ApJ*, 755, 145
 Hayashi, K. & Chiba, M. 2015, *ApJ*, 810, 22
 Hayashi, K., Ichikawa, K., Matsumoto, S., et al. 2016, *MNRAS*, 461, 2914
 Hui, L. 2001, *Physical Review Letters*, 86, 3467
 Irwin, M. & Hatzidimitriou, D. 1995, *MNRAS*, 277, 1354
 Jing, Y. P. & Suto, Y. 2002, *ApJ*, 574, 538
 Kim, S. Y., Peter, A. H. G., & Hargis, J. R. 2018, *Physical Review Letters*, 121, 211302
 Klypin, A., Kravtsov, A. V., Valenzuela, O., & Prada, F. 1999, *ApJ*, 522, 82
 Kowalczyk, K., Łokas, E. L., & Valluri, M. 2017, *MNRAS*, 470, 3959
 Kowalczyk, K., Łokas, E. L., & Valluri, M. 2018, *MNRAS*, 476, 2918
 Massari, D., Breddels, M. A., Helmi, A., et al. 2018, *Nature Astronomy*, 2, 156
 Mateo, M. L. 1998, *ARA&A*, 36, 435
 McConnachie, A. W. 2012, *AJ*, 144, 4
 Merrifield, M. R. & Kent, S. M. 1990, *AJ*, 99, 1548
 Moore, B., Ghigna, S., Governato, F., et al. 1999, *ApJ*, 524, L19
 Navarro, J. F., Frenk, C. S., & White, S. D. M. 1996, *ApJ*, 462, 563
 Press, W. H., Teukolsky, S. A., Vetterling, W. T., & Flannery, B. P. 1992, *Numerical Recipes: The Art of Scientific Computing*, 2nd edn. (New York, NY, USA: Cambridge University Press)

Richardson, T. & Fairbairn, M. 2013, MNRAS, 432, 3361
Schwarzschild, M. 1979, ApJ, 232, 236
Schwarzschild, M. 1993, ApJ, 409, 563
Strigari, L. E., Frenk, C. S., & White, S. D. M. 2017, ApJ, 838, 123
Strigari, L. E., Koushiappas, S. M., Bullock, J. S., et al. 2008, ApJ, 678, 614
van den Bosch, R. C. E., van de Ven, G., Verolme, E. K., Cappellari, M., & de Zeeuw, P. T. 2008, MNRAS, 385, 647
Vera-Ciro, C. A., Sales, L. V., Helmi, A., & Navarro, J. F. 2014, MNRAS, 439, 2863
Vogelsberger, M., White, S. D. M., Helmi, A., & Springel, V. 2008, MNRAS, 385, 236
Walker, M. G., Mateo, M., & Olszewski, E. W. 2009a, AJ, 137, 3100
Walker, M. G., Mateo, M., Olszewski, E. W., et al. 2007, ApJ, 667, L53
Walker, M. G., Mateo, M., Olszewski, E. W., et al. 2009b, ApJ, 704, 1274
Walker, M. G., Olszewski, E. W., & Mateo, M. 2015, MNRAS, 448, 2717
Wetzel, A. R., Hopkins, P. F., Kim, J.-h., et al. 2016, ApJ, 827, L23
Wolf, J., Martinez, G. D., Bullock, J. S., et al. 2010, MNRAS, 406, 1220
Zolotov, A., Brooks, A. M., Willman, B., et al. 2012, ApJ, 761, 71

Appendix A:

Generating a mock dataset with realistic errors

Like in Breddels et al. (2013), we define v_i as the true line-of-sight velocity of star i and ϵ_i as the (true and unknown) measurement error on that star. Therefore $v_i + \epsilon_i$ is the observed velocity of star i . We note that the expectation values for the moments of the measurement errors, which are drawn from a Gaussian distribution with $\sigma = 2$ km/s, are given by: $E[\langle \epsilon_i^n \rangle] = E[\epsilon_i^n] = 0$ for odd n and $s_n \equiv E[\langle \epsilon_i^n \rangle] = E[\epsilon_i^n] = (n-1)!!\sigma^n$ for even n . In our terminology, $\hat{\mu}_n = E[\langle v_i^n \rangle] = E[v_i^n]$ denotes the true n^{th} moment, μ_n is its estimator and the observed n^{th} moment is $m_n = \frac{1}{N} \sum_{i=1}^N (v_i + \epsilon_i)^n$ for a sample of N stars in a given positional bin on the sky (i.e. kinematic-bin).

Since we want to know the true value of the moments, i.e. without measurement errors, we will compute the estimators of the true moments. We will also use raw moments (i.e. not taken about the mean velocities), and in what follows, we thus refer to ‘moments’ to denote ‘raw moments’. Since we can only in practise compute the estimators of the true moments, we replaced $\hat{\mu}_n$ by μ_n in the right-hand side of the following equations. The first four moment estimators are then given by:

$$\mu_1 = \frac{1}{N} \sum_{i=1}^N (v_i + \epsilon_i), \quad (\text{A.1})$$

$$\mu_2 = \frac{1}{N} \sum_{i=1}^N (v_i + \epsilon_i)^2 - s_2, \quad (\text{A.2})$$

$$\mu_3 = \frac{1}{N} \sum_{i=1}^N (v_i + \epsilon_i)^3 - 3\mu_1 s_2, \quad (\text{A.3})$$

and

$$\mu_4 = \frac{1}{N} \sum_{i=1}^N (v_i + \epsilon_i)^4 - 6\mu_2 s_2 - 3s_2^2. \quad (\text{A.4})$$

To compute the error on these moments, we compute the square root of the variance of the moments; $Var(\hat{\mu}_n) \approx Var(\mu_n) \approx Var(m_n) = E[m_n^2] - (E[m_n])^2$:

$$\begin{aligned} Var(\mu_1) &= \frac{\mu_2 + s_2 - \mu_1^2}{N} \\ &= \frac{1}{N} \left\{ \frac{1}{N} \sum_{i=1}^N (v_i + \epsilon_i)^2 - \left[\frac{1}{N} \sum_{i=1}^N (v_i + \epsilon_i) \right]^2 \right\}, \end{aligned} \quad (\text{A.5})$$

$$\begin{aligned} Var(\mu_2) &= \frac{1}{N} \left[\mu_4 - \mu_2^2 + 4\mu_2 s_2 + 2s_2^2 \right] \\ &= \frac{1}{N} \left\{ \frac{1}{N} \sum_{i=1}^N (v_i + \epsilon_i)^4 - \left[\frac{1}{N} \sum_{i=1}^N (v_i + \epsilon_i)^2 \right]^2 \right\}, \end{aligned} \quad (\text{A.6})$$

$$\begin{aligned} Var(\mu_3) &= \frac{1}{N} \left[\mu_6 + 15\mu_4 s_2 + 45\mu_2 s_2^2 + 15s_2^3 - \mu_3^2 \right. \\ &\quad \left. - 6\mu_3 \mu_1 s_2 - 9\mu_1^2 s_2^2 \right] \\ &= \frac{1}{N} \left\{ \frac{1}{N} \sum_{i=1}^N (v_i + \epsilon_i)^6 - \left[\frac{1}{N} \sum_{i=1}^N (v_i + \epsilon_i)^3 \right]^2 \right\}, \end{aligned} \quad (\text{A.7})$$

and

$$\begin{aligned} Var(\mu_4) &= \frac{1}{N} \left[\mu_8 + 28\mu_6 s_2 - \mu_4^2 - 12\mu_4 \mu_2 s_2 + 204\mu_4 s_2^2 \right. \\ &\quad \left. - 36\mu_2^2 s_2^2 + 384\mu_2 s_2^3 + 96s_2^4 \right] \\ &= \frac{1}{N} \left\{ \frac{1}{N} \sum_{i=1}^N (v_i + \epsilon_i)^8 - \left[\frac{1}{N} \sum_{i=1}^N (v_i + \epsilon_i)^4 \right]^2 \right\}. \end{aligned} \quad (\text{A.8})$$

where the errors on the third and fourth moment estimators also depend on:

$$\mu_6 = \frac{1}{N} \sum_{i=1}^N (v_i + \epsilon_i)^6 - 15\mu_4 s_2 - 45\mu_2 s_2^2 - 15s_2^3, \quad (\text{A.9})$$

and

$$\mu_8 = \frac{1}{N} \sum_{i=1}^N (v_i + \epsilon_i)^8 - 28\mu_6 s_2 - 210\mu_4 s_2^2 - 420\mu_2 s_2^3 - 105s_2^4. \quad (\text{A.10})$$

Obviously the errors on the moments decrease when the number of stars in a kinematic-bin increases.

Appendix B: The effect of the sampling of line-of-sight velocities

In the main paper we have drawn samples of line-of-sight velocities that follow the light distribution of the mock galaxy. Here we show the results of applying the Schwarzschild modelling technique to a dataset consisting of 10^5 stars, but this time distributed such that each kinematic-bin has an equal number of stars.

Fig. B.1 presents the inference on the mass and flattening parameter and should be compared to Fig. 2 and 3. As can be observed, we have very similar inferences with the best-fit flattening parameter slightly moved into the direction of the input/true flattening value. Nonetheless, this remains fairly unconstrained.

Appendix C: Regularisation

The solution of our minimisation problem may result in a distribution of orbital weights that is rapidly varying or shows sharp discontinuities. Such a distribution would not be physical. Therefore we make the distribution of the orbital weights smoother by adding extra terms to the χ^2 -fitting algorithm such that a new quantity $\widetilde{\chi}_{\text{tot}}^2$ is minimised:

$$\widetilde{\chi}_{\text{tot}}^2 = \chi_{\text{tot}}^2 + \chi_{\text{reg}}^2. \quad (\text{C.1})$$

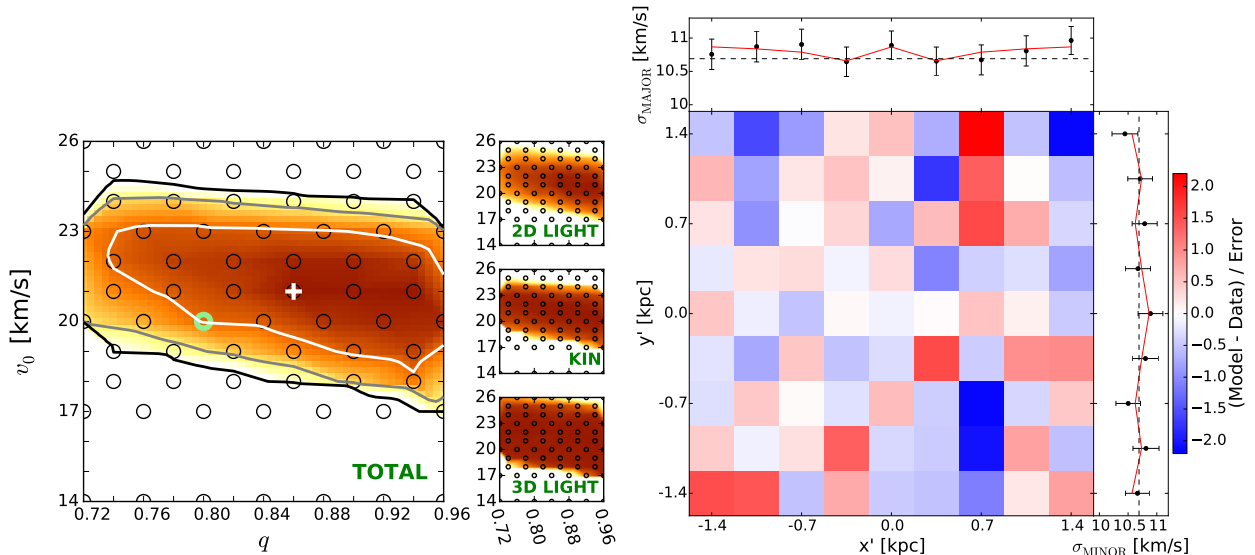


Fig. B.1. Left: The confidence intervals after fitting the Evans models to a new realization of the dataset containing 10^5 stars. This time we ensure an equal number of stars per kinematic-bin. The inference on the mass parameter remains the same. The flattening parameter remains unconstrained but has slightly shifted into the direction of the correct flattening parameter. Right: The velocity dispersion profile for the best-fit model q86v21.

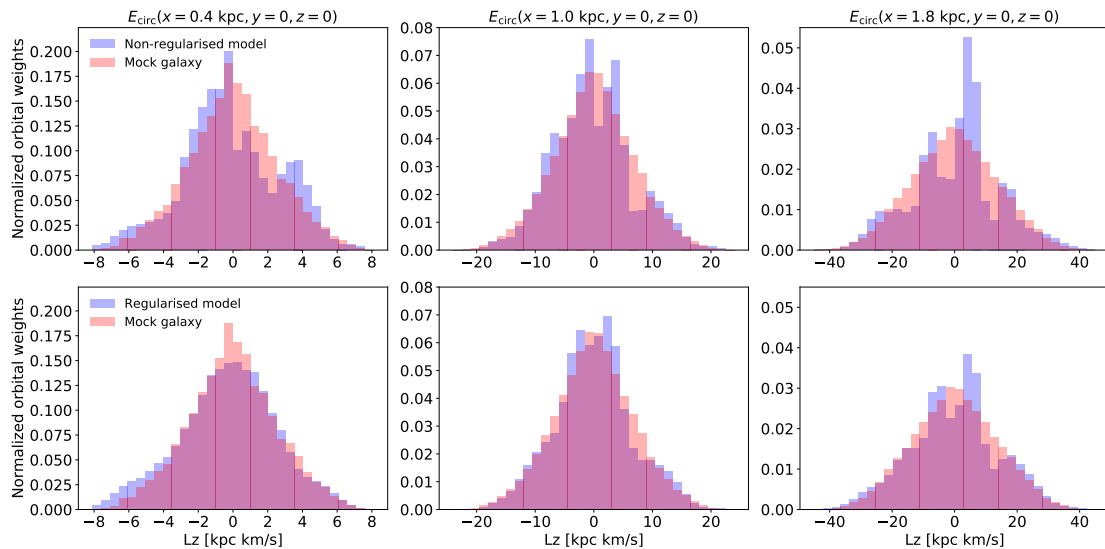


Fig. C.1. Orbital distributions of angular momentum around the symmetry axis, i.e. L_z for fixed energy slices corresponding to circular orbits at $x = 0.4$ (left), $x = 1.0$ (middle), and $x = 1.8$ kpc (right). Note the different axes ranges for the panels of each column. In the top row we show the distributions for the true Evans model q80v20 (blue) obtained for a dataset of 10^5 stars (see Sect. 4.1) and for a realization of the mock galaxy (red, here containing 4×10^5 stars in total). The effect of adding regularisation to the fit is shown in the bottom panels. Adding regularisation makes the recovered distribution smoother and more similar to the true distribution.

This procedure is called regularisation. The regularisation strength is chosen such that the orbital weights are forced to change smoothly from one neighbouring orbit to the next, while finding similar values for the best-fit characteristic parameters. In addition, the confidence contours should not be significantly shaped by the χ^2_{reg} -term. We refer the reader to van den Bosch et al. (2008) for more information about the exact implementation, in particular to Eqs. 28 and 29 of that paper. These equations require the 3-dimensional stellar density profile. For this work we assumed to know ρ_{lum} (see Eq. 2). In reality one needs the inclination angle to transform the observed surface brightness profile into the stellar density profile.

In the bottom panels of Fig. C.1, we show the effect of adding regularisation for the Evans q80v20 model (i.e. this is

the true model) on the distribution of angular momentum around the symmetry axis (L_z). The distributions can be compared to those of the q80v20 model without regularisation (top rows). We here show the example with 10^5 stars with line-of-sight velocities. The modelled distribution functions (blue) are generally smoother when regularisation is used. As a reference we also include the distributions for a realization of the mock galaxy (red). The model reproduces the mock distribution reasonably well, though some differences exist. The fact that only $\sim 30\%$ of the total number stars of the mock galaxy end up in our FOV might play a role here, in addition to the fact that we have discretized the data (by using kinematic-bins, and by modelling only the first four velocity moments).